



Stable Micelles Based on a Mixture of Coiled-coils: The Role of Different Oligomeric States

Journal:	<i>Nanoscale</i>
Manuscript ID	NR-ART-12-2017-009695.R1
Article Type:	Paper
Date Submitted by the Author:	16-Feb-2018
Complete List of Authors:	Ma, Dan; Northwestern University Keten, Sinan; Northwestern University, Mechanical Engineering

Stable Micelles Based on a Mixture of Coiled-coils: The Role of Different Oligomeric States

Dan Ma^a, Sinan Keten^{*a,b}

Homomeric micelles with tunable size, shape and stability have been extensively studied for biomedical applications such as drug carriers. However, designing the local valency and self-assembled morphology of nanophase-separated multicomponent micelles with varied ligand binding possibilities remains challenging. Here, we present micelles self-assembled from amphiphilic peptide-PEG-lipid hybrid conjugates, where the peptides can be either 3-helix or 4-helix coiled-coil. We demonstrate that the micelle size and sphericity can be controlled based on the coiled-coil oligomeric state. Using theory and coarse-grained dissipative particle dynamics (DPD) simulations in an explicit solvent simulation, we studied the distribution of 3-helix and 4-helix conjugates within the mixed micelles and observed self-organization into nanodomains within the mixed micelle. We discover that the phase separation behavior is dictated by the geometry mismatch in alkyl chain length from different coiled-coil oligomeric states. Our analyses on the self-assembly tendency and drug delivery potency of mixed micelles with controlled multivalency provide important insights into the assembly and formation of nanophase-separated micelles.

Introduction

Micelle based on hybrid block copolymers has emerged as a new platform for nanocarriers that achieve tumor-selective macromolecular drug targeting via the enhanced permeation and retention (EPR) effect¹⁻⁵. The major challenge for drug targeting is to acquire precise targeting and high delivery efficiency while avoiding non-specific binding and steric interferences from biological barriers. A tunable ligand density is necessary to strengthen the ligand-receptor binding while avoiding entropic repulsion.⁶⁻⁹ Controlling the number of copies of ligands on the nanocarrier surface as well as their location is necessary to improve the targeting efficiency of nanocarriers through multivalent linkages that allow more targeted cell internalization.¹⁰⁻¹³ Meanwhile, microphase segregation in micelles can be used to control not only the spatial distribution of ligands, but also the self-assembly characteristics of the bulk nanostructure.¹⁴ However, in contrast to multicomponent lipid mixtures that have a well characterized phase separation behavior in membranes¹⁵⁻²⁰, there are limited reports on nanophase-separated micelles that employ hybrid polymer-peptide conjugates. In analogy with cell membranes, domain budding is shown to depend on the geometric features of the lipid units such as height, and it is expected that similar features with possibly greater diversity exist in hybrid biomaterials as well.^{21, 22} A new design of 3-helix micelle (3HM) nanocarrier based on amphiphilic peptide-PEG-lipid conjugates²³⁻³⁰ is reported to have the potential to provide control over the local multivalency of presented ligand clusters. Polyethylene glycol (PEG), which has good hydrophilic properties and biocompatibility, has been shown to stabilize the secondary and tertiary structure of peptides regardless of PEG conjugation site and density^{26, 31-33}. Recent simulation studies discovered that the micelle size and stability were dictated by a combined effect of the confinement of PEG chains under micelle morphology and the intermolecular cohesive interaction among PEG chains²⁹. While these micelles form well-

defined shapes and their size can be controlled through tuning parameters such as PEG chain length, means to control the density, distribution and orientation of ligands on the particle surface remain limited with existing designs. To this end, amphiphilic peptide-PEG-alkyl conjugates based on different coiled-coil oligomeric states offer the possibility to create multicomponent micelles with control over the availability of ligand binding sites. In the work by Ang et al.³⁴, the formation of self-assembled patchy micelles from mixtures of trimeric and tetrameric coiled coils was observed through differential scanning calorimetry, fluorescence recovery spectroscopy, and coarse-grained molecular dynamics simulation. It was found that the mixed micelles had high stability in serum albumin with controlled cluster size and local multivalency. However, the driving force of the phase separation shown in mixed micelles was not characterized in detail.

In this work, we sought to explain our previously reported self-organization of patchy phases in mixed coiled-coil micelles as a step towards prospecting them as nanocarriers. Herein, we used coarse-grained molecular dynamics (MD) simulations to investigate the self-assembly of amphiphilic coiled-coil peptide-PEG-lipid hybrid conjugates based on different coiled-coil oligomeric states. Specifically, we examined how micelles formed from 4-helix based conjugates compared to 3-helix based conjugates in terms of self-assembly kinetics as well as micelle size and shape. We revealed differences in the conformation of alkyl chains under varied coiled-coil oligomeric states through a systematic characterization of the micelle structures. This analysis uncovered that alkyl chain geometry and packing govern phase separation, where steric restrictions were further quantified by measuring alkyl chain extension in each case. We also demonstrated variations of micelle stability and self-assembly tendency by calculating the interaction energy between alkyl chains under different oligomeric states. Size and hydrophobicity of the formulated micelles were also quantified to see if micelles could be suitable for penetrating biological barriers. We anticipate that our findings can help understand the phase separation behavior in mixed micelles with different oligomeric states and provide guidance to develop biomaterials with controlled local multivalency for tunable stability, shape and drug loading potency as nanocarriers.

^a Department of Mechanical Engineering, Northwestern University, Evanston, Illinois 60208.

^b Department of Civil and Environmental Engineering, Northwestern University, Evanston, Illinois 60208.

* Corresponding author: s-keten@northwestern.edu

Materials and Methods

The molecular dynamics simulations presented in this work included all-atomistic (AA) simulations and coarse-grained (CG) simulations based on the dissipative particle dynamics (DPD) technique. We first conducted AA simulations for studying the conformational behaviors of alkyl chains on an isolated coiled-coil in explicit water solvent. Considering the length and time-scale limitations of AA simulations, we chose to utilize a DPD^{35,36} coarse-grained simulation methodology for micelle formation simulations. DPD is a Lagrangian thermostat technique that enables fast coarse-grained simulations by employing hydrodynamics preserving interactions to describe phase separation in materials. This method has been widely used in studying the behavior of lipid membranes³⁷⁻³⁹. In this research, we adopted the lipid model developed by Groot and Rabone⁴⁰, PEG model developed by Ying³⁹, and peptides model developed by us in our previous publications^{23,29}. Previously, micelles were shown to be stable *in vitro* and *in vivo* when a drug or radiotherapy agent was attached to validate the 3-helix micelles as an effective drug carrier.^{28,30} Here, since we focus on micelle characteristics, we did not include drug molecules in our model to maintain generality and computational efficiency.

The two kinds of amphiphilic conjugates in AA simulations are schematically shown in Figure 1(b)(d). The headgroup of both amphiphiles is composed of a peptide-polyethylene glycol (PEG) conjugate, in which the peptides are coiled-coils consisting of three alpha helical strands in Figure 1(b) or four alpha helical strands in Figure 1(d). The atomistic structure of trimer or tetramer coiled-coil is available in the Protein Data Bank, referred as '1coi' for the trimeric helix and '1m3w' for tetrameric helix. To enable coupling of maleimide end-functionalized PEG, we performed S14C and K14C mutations on 3-helix strand and 4-helix strand respectively. PEG chain with constant degree of polymerization DP = 44 (molecular weight ~ 2000 Da) is conjugated on residue 14 of each helix. Two C16 alkyl chains are attached to the peptide N-terminus through Glutamic (GLU) residue as tail of the amphiphile, with a 6-aminohexanoic acid linker inserted between peptide and alkyl chains.

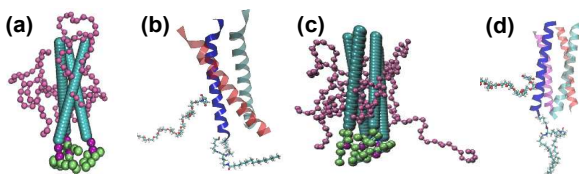


Figure 1. Schematic figure of MD models used in simulations (a) 3-helix bundle (cyan) in CG DPD model with the PEG chain (pink) and the alkyl chain (purple and green) conjugated to each strand. (b) 3-helix bundle in AA model. For simplicity, only PEG (CPK drawing method) and alkyl (Licorice drawing method) chain conjugated to the blue helix bundle are shown here. (c) 4-helix bundle (cyan) in CG DPD model with the PEG chain (pink) and the alkyl chain (purple and green) conjugated to each strand. (d) 4-helix bundle in AA model. For simplicity, only PEG (CPK drawing method) and alkyl (Licorice drawing method) chain conjugated to the blue helix bundle are shown here.

All the AA simulations were performed using NAMD⁴¹ under an NPT ensemble with a constant pressure of 1 atm and a constant temperature at 300 K. The amphiphiles were solvated in an explicit water solvent using the TIP3P water model⁴², and periodic boundary conditions were applied in the three dimensions. The bonded interactions were modeled using the CHARMM force field⁴³, long-range nonbonded interactions were modeled using the standard Lennard-Jones potential, and the particle-mesh Ewald technique were used for electrostatics interactions. The minimization of the systems run for 50,000 steps and was followed by a 1 ns equilibrium simulation using a 1 fs timestep. The equilibrium of the simulation system was assured by checking the convergence of the radius of gyration and end-to-end distance of alkyl chains.

In DPD simulations, three pairwise forces act as interactions among bead *i* and *j*: a conservative force F_{ij}^C , a dissipative force F_{ij}^D , and a random force F_{ij}^R .

$$F_i = \sum_{j \neq i} F_{ij}^C + F_{ij}^D + F_{ij}^R, \quad r_{ij} < r_c \quad (1)$$

The conservative force is a soft repulsion term of the form $F_{ij}^C = a_{ij} \omega(r_{ij}) \hat{r}_{ij}$, where $\omega(r_{ij})$ is a normalized distribution function:

$$\omega(r_{ij}) = \begin{cases} 1 - \frac{r_{ij}}{r_c} & (r_{ij} < r_c) \\ 0 & (r_{ij} \geq r_c) \end{cases} \quad (2)$$

and a_{ij} is the maximum repulsion, which can be derived from the Flory-Huggins theory of polymers. The interactions between different particles used in the presented simulations as well as their validation can be found in our previous publications.^{23,29}

The other two forces have the forms $F_{ij}^D = -\gamma \omega^2(r_{ij}) (\hat{r}_{ij} \cdot \dot{v}_{ij}) \hat{r}_{ij}$ and $F_{ij}^R = \sigma \omega(r_{ij}) \alpha \delta t^{-1/2} \hat{r}_{ij}$. They serve as heat sink and heat source respectively and keep the thermostat of the system.^{37,39} α is a Gaussian random number with zero mean and unit variance, $\delta t = 0.006\tau$ is the timestep. Random noise parameter $\sigma = 3$, dissipation parameter $\gamma = 4.5$ were taken from the work of Groot et al. and they related to each other as $\sigma^2 = 2\gamma k_B T$.³⁶

Here we employed the same mapping method for CG simulations as we did in our previous study on 3-helix micelle, which has improved its efficiency and accuracy in predicting peptide-PEG micellization behavior.^{23,29} All CG simulations in this work were performed using a variation of the DPD approach, with the open source MD simulation package LAMMPS⁴⁴. An NVT ensemble with a constant temperature 300 K was adopted for simulations, and periodic boundary conditions were applied in the three dimensions. Here the time scale is $\tau = 24.32 ps$, length scale is $R_C = 0.8 nm$.^{37,39} We investigated systems with 3-helix amphiphiles, 4-helix amphiphiles and a mixture of the amphiphiles. To reduce sampling errors, we carried out 3 duplicate simulations with different random seeds for each case. Each simulated system consists of 100 randomly distributed amphiphilic molecules (the mixture system had 50 amphiphilic molecules for each type), and then solvated in explicit DPD water beads. All CG simulations were carried out for approximately $2.0 \mu s \sim 2.8 \mu s$, and tended to reach equilibrium before 800 ns. The equilibration of the simulations was assured by checking that the average micelle aggregation number was a stable value that does not decrease or increase by more than 3 in 200 ns. The last 150 ns of the whole simulations were chosen for data analyses.

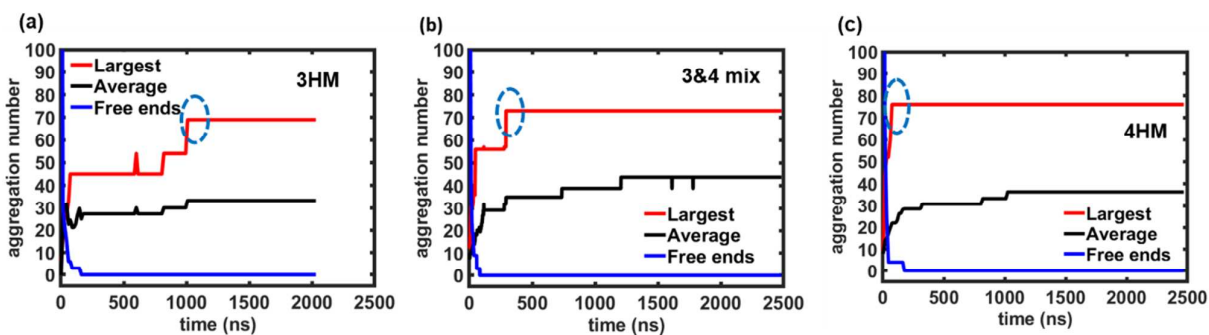


Figure 2. The number of free subunits in system and the largest, average aggregation number defined as the number of helices in the (a) 3HM, (b) 3&4 mixture micelle, and (c) 4HM as a function of time. The sharp increases indicating micelle fusion process are highlighted in dashed blue ovals. The results are obtained from DPD CG simulations with 100 subunits for each case.

For the theoretical investigation on the phase separation, sample micelles with 3 different 3helix:4helix ratios were chosen for fragmentation frequency distribution analysis (similar to MALDI spectra^{45, 46}). Here all the possible 8-bead-fragmentations in the sample micelles were classified according to the number of 3-helix component beads (from 0 to 8). The size of the fragmentation here was chosen because the total number of beads in the double alkyl chain except for connection beads was 8. To quantify micro-phase separation, we compared the fragmentation density distribution of sample micelles with a random model and calculated the sum-of-squares error to provide a metric for phase separation.

Results and discussions

First, we present DPD CG simulations that investigate micelle formation behaviors for 3HM, 4HM and 3&4 mixture micelles, given the same initial subunit concentration in each system. The driving force of all three kinds of micelle formation processes is the hydrophobic effect induced by the explicit water solvent molecules, which interact unfavorably with the alkyl chains. This effect causes the subunits to aggregate into larger clusters with the hydrophobic alkyl chains forming the micelle core and hydrophilic PEGylated peptides forming the shell. The most common simulation outcome for all three different cases is the formation of spherical micelles.

To quantify micelle size and formation kinetics, we look at two metrics, the average micelle size and the largest micelle size. Here the micelle size refers to aggregation number, i.e. the number of helices in each micelle. We observe similar micelle sizes for the three different kinds of micelles as shown in Figure 2. However, the simulation time that each system takes to form the largest micelle varies, suggesting that the subunits exhibit different kinetics of self-assembly. More specifically, 3HM takes the longest time to form its largest micelle (approximately 1000 ns on average), while 4HM takes the shortest time (approximately 130 ns on average), and 3&4 mixture micelle lies in between (approximately 250 ns on average), as shown in SI Figure 1. Under the hydrophobic driving force, an individual micelle can increase its size by either combining with free subunits nearby or by fusing with other neighboring micelles. To explain the differences witnessed in the largest micelle formation time, we investigate the micelle growth behavior under these two conditions respectively. As shown in Figure 2(a), the largest micelle size in 3HM increases twice sharply (highlighted in blue oval),

indicating that micelle fusion happens at around 800 ns and 1000 ns respectively. Regarding 3&4 mixtures and 4HM cases, we observe similar micelle fusion processes, but they occur much earlier in the simulation, at around 300 ns for 3&4 mixture micelle and at around 100 ns for 4HM respectively as shown in Figure 2(b) and (c). A possible explanation to this phenomenon is the fact that 4HM has a stronger hydrophobic driving force due to higher alkyl monomer density and tighter packing. On the other hand, we also observe the number of free subunits in system decrease to 0 before 200 ns for all the three cases as shown in Figure 2, which indicates that no more free subunits are available to join formed micelles. Beyond this early aggregation phase, the dominant mechanism of micelle size increase are the fusion events. In summary, the 4HM has the fastest micelle formation process resulting in the largest micelles, due to a combined effect of a stronger hydrophobic driving force and better packing efficiency at its core to form a spherical micelle. These effects are also present in 3&4 mixture micelles, and thus influence the shape of the mixed micelles and accelerate their formation process.

As discussed above, one of the major differences in the micelle formation processes between 3HM and 4HM is that, the 4HM appears to have a stronger hydrophobic driving force. In order to study the alkyl chain density and provide an explanation for the difference in hydrophobic interactions, we study the conformational behavior of alkyl chains on isolated subunits and in micelles using CG DPD simulations. We also corroborate these results with AA simulations that examine the conformational behavior of alkyl chains on an isolated subunit in solution. As shown in Table 1 below, both simulation methods reach the same conclusion that the alkyl chains on isolated 3-helix subunit bundle or in 3HM have less extended conformations than those on isolated 4-helix or in 4HM. The alkyl chains in CG DPD simulations are shorter than those in AA simulations because they have fewer degrees of freedom in CG DPD simulations than in AA simulations, and thus exhibit less steric hindrance. For star shaped polymers, M. Daoud et al. reported that if the number of polymers is sufficiently high, the structure of each polymer is stretched due to confinement effects⁴⁷. This theory can be used to explain our observations on micelle core size: the alkyl chains in 4HM are slightly extended due to higher packing density than in 3HM.

To study the packing density of alkyl chains, we plot the conformational distribution of alkyl chains on the cross-sectional

		3HM		4HM		3-helix components in mixture		4-helix components in mixture	
		R_g (Å)	R_{ee} (Å)	R_g (Å)	R_{ee} (Å)	R_g (Å)	R_{ee} (Å)	R_g (Å)	R_{ee} (Å)
On isolated helix bundle	AA	4.9 ± 0.2	12.5 ± 1.0	5.0 ± 0.1	14.0 ± 0.6				
	CG DPD	4.1 ± 0.1	10.7 ± 0.4	4.7 ± 0.2	11.5 ± 0.5				
In micelle	CG DPD	4.2 ± 0.1	11.2 ± 0.1	4.9 ± 0.1	12.1 ± 0.2	4.3 ± 0.1	11.2 ± 0.1	4.9 ± 0.1	12.1 ± 0.2

Table 1. Average conformational size of alkyl chains, including radius of gyration R_g and end-to-end distance R_{ee} in DPD simulations. The results in table are given by the present DPD CG simulations for alkyl chains in 3HM, 4HM and 3&4 mixture micelle, alkyl chains on the isolated 3-helix or 4-helix, and compares the CG DPD and AA simulation results for alkyl chains on isolated 3-helix and 4-helix.

plane as shown in Figure 3. Note that alkyl chains in both cases have the highest probabilities within the boundary marked by the conjugation points and at the center of the helix bundle, indicating the fact that alkyl chains have relatively high attraction between each other. Comparing a 3-helix vs. 4-helix sample micelle with the same number of subunits, 4HM has much higher values of the probability distribution in its center than 3HM due to the larger number of beads in the sample micelle with the same number of subunits. Comparing Figure 3(b) for the distribution area of alkyl chains in 3HM and Figure 3(c) for 4HM, we can conclude that the alkyl chains have very similar area distribution sizes for each subunit. Considering a distribution probability larger than 1×10^{-4} to define the area, 3HM displays a distribution area size of 1.58 nm^2 on xy plan, while 4HM displays a slightly larger area size of 1.80 nm^2 . Since 6 alkyl chains are conjugated on a 3-helix while 8 alkyl chains are conjugated on a 4-helix, we saw a higher alkyl chains concentration for 4HM (4.46 chains/nm^2) than for 3HM (3.80 chains/nm^2). This explains the fact that 4HM has larger aggregation number and better stability. With increase in alkyl chain length, there is a corresponding higher hydrophobic interaction between alkyl chains in the micelle formation process.

Next, we present an analysis of the packing behavior of the 3-helix and 4-helix components in 3&4 mixture micelles. Combined with

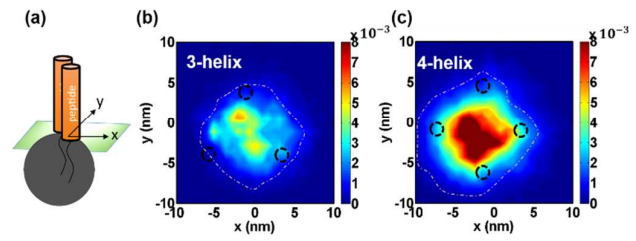


Figure 3. Distribution behavior of alkyl chains on the helix bundle cross section plane in micelles, including alkyl chains conjugated on (b) 3-helix peptide and (c) 4-helix peptide. A schematic figure (a) on left shows the axis setting method in both figures: with the alkyl bead distribution projected onto the xy plane that is orthogonal to the helix bundle (radial) direction. In the figure (b)(c), the color bars in show the probability distribution decrease from red to blue, the black dashed in indicate the estimated conjugation location on helix terminus, and the orange point dash lines indicate alkyl chain distribution area that has a probability density value larger than 1×10^{-4} . The results are given by the present DPD CG simulations for 3HM and 4HM sample micelles with the same number of subunits over the last 150 ns after convergence.

experimental observations³⁴ and phase separation analysis presented in Figure 4, we can conclude that the 3-helix and 4-helix components have a phase separation behavior in their mixture. Typically, experimental techniques such as MALDI are used to quantify micro-phase separation, where comparison with a binomial (random) model and subsequent calculation of the sum-of-squares error provides a metric for phase separation. The same analysis can be done on the simulated systems to quantify microphase separation. From the analysis of the trajectories, we find that the 3-helix subunits tend to assemble into a hemisphere of the mixture micelle, while 4-helix subunits assemble into the other hemisphere of the mixture micelle. The phase separation behavior shown here is more clear than what were reported in the previous copolymer self-assembly phase separation behaviors^{48,49}, because the assembled subunits in our system have relatively large subunit volume. To differentiate the effects of core and shell, we first calculate the radius of gyration and end to end length of PEG in free solution, on isolated 3-helix bundle, in 3HM and in 4HM as in SI Table 1. The PEG chains have very similar

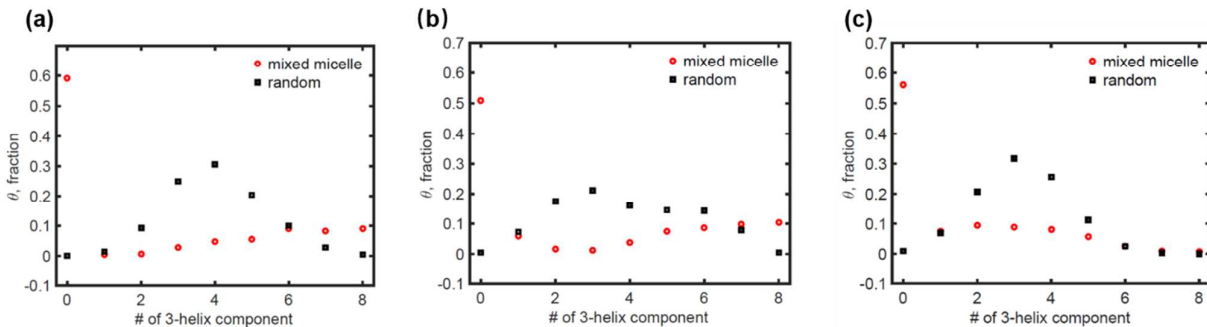


Figure 4. Phase separation and fragmentation measurements (red) compared to well mixed theoretical micelles (black) for three sample micelles (a-c). Panels (a-c) show θ , the number fraction of 8-bead fragmentation as a function of the number of 3-helix component in the 8 beads. The aggregation number of the sample micelles are 50, 56 and 57, with 3helix:4helix ratio 6:8, 8:8 and 7:8 respectively. The calculated sum of squared error (SSR) are high as 0.504, 0.438 and 0.492, which are anticipated for phase separated mixed micelles.

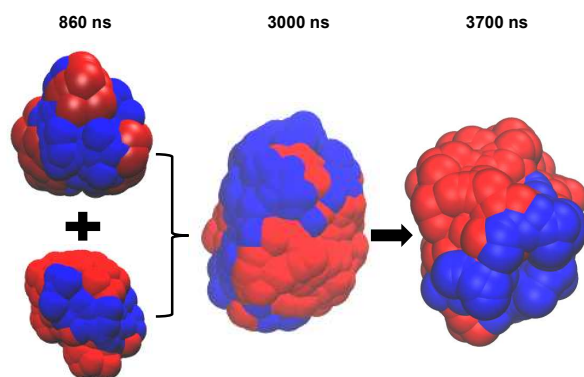


Figure 5. Schematic figure of the micelle fusion process, with the initial configuration of the small micelles at 860 ns, and the merged micelle at 3000 ns and 3700 ns. This figure shows the migration of coiled-coils into nanodomains within the mixed micelle. Only alkyl chains are shown in this figure for simplicity, with 4-helix components in red and 3-helix components in blue.

behavior in 3HM and 4HM, which excludes the possibility that PEG can be the driving force of phase separation. Combined with the aforementioned analysis on conformational behaviors of alkyl chains, we can conclude that the alkyl chains from different components phase separate in the cores during micelle formation process and thus lead to the phase separation in the whole micelle. More specifically, due to the favorable interaction between alkyl beads, the alkyl chains prefer to assemble with other alkyl chains which have similar conformational distribution and length. As such, subunits from the same components assemble quickly into clusters. It should be noted that in Figure 4 (a)(b)(c), the fractions of all 4-helix component fragmentations are dominant, which indicates that the rapid self-assembly process of 4-helix components leads to the phase separation in mixed micelles, while the 3-helix components fill up the

rest of the space. In the micelle fusion process, small micelles with phase separation behavior merge into a larger cluster with the phase separation behavior preserved, as shown in Figure 5. We can also conclude from the visualization of the simulation trajectories that fusing with other neighboring micelles is the dominant route to increase the size of individual micelles. Subunit migration is observed during the micelle fusing process as shown in Figure 5.

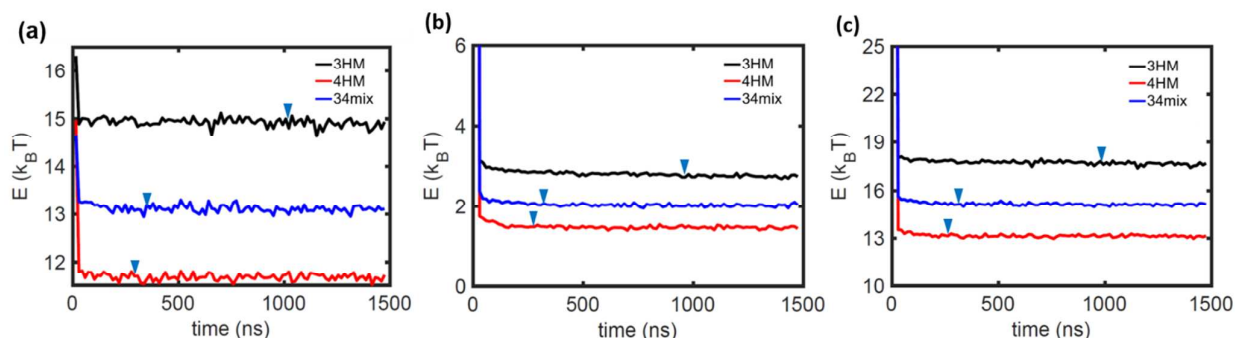


Figure 6. Average interaction energy between alkyl beads and (a) alkyl beads, (b) other beads, including peptide, PEG and water, (c) all beads as a function of simulation time. This energy function compares pure 3-helix micelle (black), pure 4-helix micelle (red) and 3&4 mixture micelles (blue). The blue triangles indicate the convergence time for the two systems, at 300 ns for 3HM, 1000 ns for 4HM, and 330 ns for 3&4 mixture micelles. The results are given by DPD CG simulations including 3HM, 4HM and mixture micelles.

Since some subunits may not find other subunits with the same

	3HM	4HM	34mix
AG number	45	60	50
Alkyl core radius (nm)	3.2	3.7	3.2
Vacancy in core (nm ³)	80.7	132.0	85.3
Micelle radius (nm)	7.0	7.7	7.4
Water content in micelle	4.2×10^3	5.3×10^3	4.5×10^3
SASA(nm ²)	18.0 ± 6.0	31.8 ± 6.8	24.1 ± 6.4

Table 2. Aggregation number, alkyl core radius, vacant volume in micelle core, water beads permeability and micelle SASA in comparison of 3HM, 4HM and 3&4 mixture micelles. The results are given by sample micelles in the present DPD CG simulations including all the three helix components. The water content in micelle is defined as the number of water beads inside the sample micelle (the micelle boundary here is defined as a PEG weight fraction at 10%).

oligomeric state nearby due to steric hindrance, some flaws and imperfect phase separation in large micelles can be seen.

Next, we present more details about the geometric characteristics of sample micelles from the DPD CG simulations as shown in Table 2 below to further investigate micelle size and hydration rate, as a step towards prospecting these nanocarriers for drug delivery applications. We can conclude from this table that, under the circumstances that each micelle has the similar number of subunits, 3HM, 4HM and 3&4 mixture micelles have comparable micelle sizes and core sizes. The 4HM has the greatest vacancy in the core and largest water content in the micelle, due to stretched alkyl structure, suggesting some packing frustration that may arise due to stronger driving forces and faster kinetics. Meanwhile, 3&4 mixture micelles have a larger vacant volume in the core than 3HM with the same alkyl core size, which may offer advantages for serving as a drug carrier. A possible explanation to this phenomenon can be that the phase separation in 3&4 mixture micelles leads to a more compact geometry with better packing. More specifically, subunits from different components separate and have different conformation distributions. This difference in distribution enlarges the vacant volume in core. As for the degree of hydration, both SASA and number of water beads permeating the micelle indicate that the 3&4 mixture micelle has a median degree of hydration in all the

three cases, while 4HM has the highest.

The orientation of the helix bundle controls the orientation of ligands conjugated to the helix end, which determines the nanoparticle surface chemistry and the availability of ligand binding sites. Characterization of the ligand availability on the surface gain additional insights into the micelle shape, which we obtain by studying the helix orientation in micelles and the principal moments of inertia^{50 51}. The average ratios of the largest to smallest principal moments of inertia (I_{max}/I_{min}) over the last 150 ns of simulations for 3HM, 4HM and 3&4 mixture micelle are 1.31 ± 0.07 , 1.47 ± 0.07 and 1.16 ± 0.05 respectively, with eccentricity ($\eta = 1 - \frac{I_{min}}{I_{avg}}$)

0.13 ± 0.03 , 0.21 ± 0.03 , 0.08 ± 0.03 respectively. We also analyze the micelles, we find the orientation for helix bundle in 3HM to be $\varphi_{3HM-pure} = 19.4^\circ$; while in 4HM, $\varphi_{4HM-pure} = 25.5^\circ$. As for 3&4 mixtures, we calculate helix bundle orientation with regards to micelle radial direction to gain further insights into the micelle sphericity. From the sample mixture micelle $\varphi_{3HM-mix} = 16.3^\circ$, $\varphi_{4HM-mix} = 18.8^\circ$, $\varphi_{avg-mix} = 17.4^\circ$. The higher helix disorientation seen in 4HM is caused by a minor angle deviation in the 4-helix bundle structure. A better helix bundle orientation indicates a more spherical micelle shape, corresponding well with the aforementioned orientation analyses. An explanation for this phenomenon may be the more efficient packing of the micelle core due to the mixing of alkyl chains from different components which resolves packing frustration by allowing irregular subunit shapes to fill up the free volume more effectively. In a recent study on the shape effect of PEGylated nanoparticles on cellular uptake, Ying Li et al. reported that spherical nanoparticles encounter minimal internalization energy changes and thus should be most efficient as drug carriers.³⁹ Based on this observation, we suggest that the higher sphericity of the 3&4 mixture micelle may make it a better nanocarrier for drug delivery applications.

In order to quantify the interaction energy for alkyl chains beads in different components, we take the soft repulsive potential between

two particles as
$$U^{rep}(r_{nm}) = \begin{cases} \frac{1}{2} a_{ij} (1 - r_{nm})^2 & \text{for } 0 \leq r_{nm} < r_c \\ 0 & \text{for } r_{nm} \geq r_c \end{cases}$$
,

where r_{nm} is the distance between bead n and m, and a_{ij} is the repulsive parameter between bead type i and j.⁵² First, the pair correlation functions between alkyl beads and all types of beads are calculated, and when implemented into the repulsive potential above, we can come up with the interaction energy for alkyl beads. Given the repulsive nature of the potential, lower numerical values of the interaction energy indicate more favorable interactions. To compare different systems, we plot the alkyl interaction with alkyl, alkyl interaction with all other types of beads (including peptide, PEG and water), and finally alkyl interaction with all the beads as a function of time in Figure 6. Comparing alkyl to alkyl interactions in 3HM and 4HM in Figure 6(a), we see that alkyl beads have more favorable interactions in 4HM. This confirms our previous conclusion that alkyl beads in 4HM have a larger driving force in micelle formation. In Figure 6(b), we see the same trend for alkyl beads and peptide, PEG and water interaction, that alkyl beads have less interaction energy to other repulsive beads. This again ascertains our previous conclusion on micelle driving forces and indicates that alkyl chains have a more extended conformation in 4HM relative to 3HM. Furthermore, we see that the alkyl energy declines continuously until convergence in Figure 6 (b)(c), which indicates that the energy decreases with self-assembly events that lead to micelle formation. In order to quantify and compare the free energy for micelle formation in 3HM, 4HM and mixture micelles, we tabulate the energy terms of sample micelles in Table 3. All the three energy terms for alkyl beads interaction energy in sample

	3HM	4HM	mixture			3-helix single	4-helix single
			Ratio= 3:4	Ratio= 7:5	Ratio= 11:5		
U_{alkyl} ($k_B T$)	14.91±0.01	11.67±0.04	12.93	13.38	13.62	15.99	13.74
U_{others} ($k_B T$)	2.63±0.02	1.28±0.02	1.74	1.93	2.08	2.74	3.23
U_{all} ($k_B T$)	17.54±0.03	12.95±0.02	14.66	15.31	15.70	18.73	16.97
ΔF ($k_B T$)	1.17±0.03	-4.02±0.02	-2.94	-2.56	-2.37		

Table 3. Alkyl beads to alkyl beads, others repulsive beads, all beads average interaction energy in sample 3HM, 4HM and mixture micelle; and alkyl beads interaction energy in 3-helix and 4-helix conjugates isolated in water solution. The free energy of 3HM, 4HM, and mixture micelle formation is also calculated as the energy in micelle minus the energy in isolated single helix bundle. The 3HM and 4HM results are given by the average and standard deviation values of 3 micelle samples with different sizes, and mixture micelles results include 3 different sample micelles with an increasing 3-helix component: 4-helix component ratio. Given that DPD has the repulsive interaction potential nature, larger interaction energy value here indicates less favorable interaction.

micelles agree well with the results in Figure 6. Moreover, we see that the free energy of 4HM formation is the largest in the three cases, while the 3HM has the least favorable free energy and mixture micelles have free energy in between. Meanwhile, increasing the ratio of 3-helix component in mixture micelles lowers the free energy value. These indicate that 4-helix conjugates have a large free energy in micelle formation, and thus lead to a faster micelle formation process, and a more stable micelle. Additionally, this energy difference also enables the phase separation behavior seen in simulations and experiments³⁴

Conclusion

Motivated by the desire to design mixed micelles with multivalent ligand cluster sizes, we show how coiled coil-alkyl amphiphiles side-conjugated with a PEG chain exhibit variation in micelle formation kinetics and morphology due to the differences in their coiled-coil oligomeric states. We demonstrated that the alkyl chains in different confinement states lead to different micelle stability properties. In mixed micelles, 3-helix and 4-helix components self-associate into nanodomains to improve alkyl chain packing. Characterization of the ligand orientation, micelle hydrophobicity and drug carrier capacity in different micelle cases revealed advantages of using mixture micelles. Additionally, the 4HM displays stronger interaction energy and higher stability than 3HM, further confirmed by the enthalpy of alkyl chains, which appears as the driving force for phase separation in mixed micelles. These analyses should provide useful guidance for the design of nanophase-separated micelles for multivalence ligand conjugation.

Acknowledgements

The authors acknowledge funding from the Office of Naval Research (Grant No. N00014-13-1-0760).

References

1. K. Greish, *Cancer Nanotechnology: Methods and Protocols*, 2010, 25-37.
2. A. K. Iyer, G. Khaled, J. Fang and H. Maeda, *Drug discovery today*, 2006, **11**, 812-818.
3. H. Maeda, *Bioconjugate Chem*, 2010, **21**, 797-802.
4. H. Maeda, H. Nakamura and J. Fang, *Advanced drug delivery reviews*, 2013, **65**, 71-79.
5. V. Torchilin, *Advanced drug delivery reviews*, 2011, **63**, 131-135.
6. D. R. Elias, A. Poloukhine, V. Popik and A. Tsourkas, *Nanomedicine: nanotechnology, biology and medicine*, 2013, **9**, 194-201.
7. C. C. Lee, J. A. MacKay, J. M. Fréchet and F. C. Szoka, *Nat Biotechnol*, 2005, **23**, 1517.
8. Z. Tang, D. Li, H. Sun, X. Guo, Y. Chen and S. Zhou, *Biomaterials*, 2014, **35**, 8015-8027.
9. J. Nicolas, S. Mura, D. Brambilla, N. Mackiewicz and P. Couvreur, *Chemical Society Reviews*, 2013, **42**, 1147-1235.
10. M. Mammen, S.-K. Choi and G. M. Whitesides, *Angewandte Chemie International Edition*, 1998, **37**, 2754-2794.
11. J. Rao, J. Lahiri, L. Isaacs, R. M. Weis and G. M. Whitesides, *Science*, 1998, **280**, 708-711.
12. J. M. Saul, A. V. Annapragada and R. V. Bellamkonda, *J Control Release*, 2006, **114**, 277-287.
13. C. E. Ashley, E. C. Carnes, G. K. Phillips, D. Padilla, P. N. Durfee, P. A. Brown, T. N. Hanna, J. Liu, B. Phillips and M. B. Carter, *Nat Mater*, 2011, **10**, 389.
14. M. Müllner and A. H. Müller, *Polymer*, 2016, **98**, 389-401.
15. D. G. Ackerman and G. W. Feigenson, *The Journal of Physical Chemistry B*, 2015, **119**, 4240-4250.
16. K. Bacia, P. Schwille and T. Kurzchalia, *P Natl Acad Sci USA*, 2005, **102**, 3272-3277.
17. S. Chiantia and E. London, *Biophysical journal*, 2012, **103**, 2311-2319.
18. A. Hammond, F. Heberle, T. Baumgart, D. Holowka, B. Baird and G. Feigenson, *P Natl Acad Sci USA*, 2005, **102**, 6320-6325.
19. R. Parthasarathy, C.-h. Yu and J. T. Groves, *Langmuir*, 2006, **22**, 5095-5099.
20. Q. Shi and G. A. Voth, *Biophysical journal*, 2005, **89**, 2385-2394.
21. A. J. García-Sáez, S. Chiantia and P. Schwille, *J Biol Chem*, 2007, **282**, 33537-33544.
22. F. A. Heberle, R. S. Petruzielo, J. Pan, P. Drazba, N. Kučerka, R. F. Standaert, G. W. Feigenson and J. Katsaras, *Journal of the American Chemical Society*, 2013, **135**, 6853-6859.
23. J. Ang, D. Ma, R. Lund, S. Keten and T. Xu, *Biomacromolecules*, 2016, **17**, 3262-3267.
24. H. Dong, N. Dube, J. Y. Shu, J. W. Seo, L. M. Mahakian, K. W. Ferrara and T. Xu, *ACS Nano*, 2012, **6**, 5320-5329.
25. H. Dong, R. Lund and T. Xu, *Biomacromolecules*, 2015, **16**, 743-747.
26. H. Dong, J. Y. Shu, N. Dube, Y. Ma, M. V. Tirrell, K. H. Downing and T. Xu, *Journal of the American Chemical Society*, 2012, **134**, 11807-11814.
27. N. Dube, J. W. Seo, H. Dong, J. Y. Shu, R. Lund, L. M. Mahakian, K. W. Ferrara and T. Xu, *Biomacromolecules*, 2014, **15**, 2963-2970.
28. N. Dube, J. Y. Shu, H. Dong, J. W. Seo, E. Ingham, A. Kheirloomoom, P.-Y. Chen, J. Forsayeth, K. Bankiewicz and K. W. Ferrara, *Biomacromolecules*, 2013, **14**, 3697-3705.
29. D. Ma, E. P. DeBenedictis, R. Lund and S. Keten, *Nanoscale*, 2016, **8**, 19334-19342.
30. J. W. Seo, J. Ang, L. M. Mahakian, S. Tam, B. Fite, E. S. Ingham, J. Beyer, J. Forsayeth, K. S. Bankiewicz, T. Xu and K. W. Ferrara, *J Control Release*, 2015, **220**, 51-60.
31. E. Hamed, D. Ma and S. Keten, *ACS Biomaterials Science & Engineering*, 2015, **1**, 79-84.
32. E. Hamed, D. Ma and S. Keten, *BioNanoScience*, 2015, **5**, 140-149.
33. E. Hamed, T. Xu and S. Keten, *Biomacromolecules*, 2013, **14**, 4053-4060.
34. J. Ang, D. Ma, B. T. Jung, S. Keten and T. Xu, *Biomacromolecules*, 2017, **18**, 3572-3580.
35. R. D. Groot, *The Journal of chemical physics*, 2003, **118**, 11265-11277.
36. R. D. Groot and P. B. Warren, *Journal of Chemical Physics*, 1997, **107**, 4423.
37. Y. Li, H. Yuan, A. von dem Bussche, M. Creighton, R. H. Hurt, A. B. Kane and H. Gao, *Proceedings of the National Academy of Sciences*, 2013, **110**, 12295-12300.
38. T. Yue and X. Zhang, *ACS Nano*, 2012, **6**, 3196-3205.
39. Y. Li, M. Kröger and W. K. Liu, *Nanoscale*, 2015, **7**, 16631-16646.
40. R. D. Groot and K. Rabone, *Biophysical journal*, 2001, **81**, 725-736.
41. J. C. Phillips, R. Braun, W. Wang, J. Gumbart, E. Tajkhorshid, E. Villa, C. Chipot, R. D. Skeel, L. Kale and K. Schulten, *Journal of computational chemistry*, 2005, **26**, 1781-1802.
42. W. L. Jorgensen, J. Chandrasekhar, J. D. Madura, R. W. Impey and M. L. Klein, *The Journal of chemical physics*, 1983, **79**, 926-935.
43. A. D. MacKerell Jr, D. Bashford, M. Bellott, R. L. Dunbrack Jr, J. D. Evanseck, M. J. Field, S. Fischer, J. Gao, H. Guo and S. Ha, *The journal of physical chemistry B*, 1998, **102**, 3586-3616.
44. S. Plimpton, *Journal of computational physics*, 1995, **117**, 1-19.
45. K. M. Harkness, A. Balinski, J. A. McLean and D. E. Cliffl, *Angewandte Chemie International Edition*, 2011, **50**, 10554-10559.
46. S. N. Merz, Z. J. Farrell, C. J. Dunn, R. J. Swanson, S. A. Egorov and D. L. Green, *ACS Nano*, 2016, **10**, 9871-9878.
47. M. Daoud and J. Cotton, *Journal de Physique*, 1982, **43**, 531-538.
48. G. Illya, R. Lipowsky and J. Shillcock, *The Journal of chemical physics*, 2006, **125**, 114710.
49. M. Laradji and P. S. Kumar, *The Journal of chemical physics*, 2005, **123**, 224902.
50. C. D. Bruce, M. L. Berkowitz, L. Perera and M. D. Forbes, *The Journal of Physical Chemistry B*, 2002, **106**, 3788-3793.
51. S. Salaniwal, S. Cui, H. Cochran and P. Cummings, *Langmuir*, 2001, **17**, 1773-1783.
52. C. Wijmans, B. Smit and R. Groot, *The Journal of chemical physics*, 2001, **114**, 7644-7654.

drug delivery potency of mixed micelles with controlled multivalency and phase separation

